Nano Energy 139 (2025) 110895

Contents lists available at ScienceDirect

Nano Energy

journal homepage: www.elsevier.com/locate/nanoen

Full paper

Design and functional verification of a flexible wireless spinal cord stimulator with spinal motion monitoring function

Zhao Peng [a,b], Zhaoxuan Niu [c], Chengjun Zeng [a], Wei Zhao [a,*], Jinsong Leng [d], Yanju Liu [a,*]

[a] Department of Astronautical Science and Mechanics, Harbin Institute of Technology (HIT), No. 92 West Dazhi Street, PO Box 301, Harbin 150001, PR China
[b] School of Future Technology, Harbin Institute of Technology (HIT), No. 92 West Dazhi Street, Harbin 150001, PR China
[c] School of Chemistry and Chemical Engineering, Harbin Institute of Technology, Harbin 150001, PR China
[d] Center for Composite Materials and Structures, Harbin Institute of Technology (HIT), No. 2 YiKuang Street, Harbin 150080, PR China

ARTICLE INFO

Keywords:
Fractal geometry design
Wireless inductive
Motion monitoring
Self-powered
Mechanically compatible

ABSTRACT

Spinal Cord Injury (SCI) poses a significant threat to the physical and mental well-being of patients worldwide, with conventional therapeutic approaches demonstrating limited efficacy in restoring neural function. To address this challenge, we propose a flexible, wireless spinal cord stimulation system equipped with spinal motion monitoring capabilities. This system integrates a wireless flexible spinal cord stimulator and a self-powered spinal motion monitor based on a triboelectric nanogenerator (TENG). The stimulator features fractal serpentine stretchable electrodes, which are mechanically compatible with spinal tissue, allowing it to accommodate spinal deformation and thereby minimizing the risk of tissue damage. The system also incorporates a wireless receiving antenna (Rx), composed of flexible capacitors and electrodes, designed to receive periodic electrical stimulation. The wireless stimulation is powered via electromagnetic coupling, eliminating the need for a battery and making the system more lightweight and multifunctional. Additionally, the spinal motion monitor enables real-time monitoring of the patient's spinal health, transmitting data via Bluetooth to assist clinicians and patients in preventing secondary injuries and optimizing rehabilitation strategies. This work presents a novel integrated medical device system that combines wireless transmission, therapeutic intervention, and health monitoring, offering a promising new avenue for advanced healthcare solutions.

1. Introduction

Spinal Cord Injury (SCI) represents a formidable challenge for the global medical community. With the increasing incidence of traffic accidents, sports injuries, and other events leading to spinal cord trauma, SCI has imposed far-reaching impacts on the physical and mental well-being of affected individuals. According to statistical data, approximately 250,000 to 500,000 new cases of SCI occur annually, while an estimated over 15 million people worldwide live with disabilities related to SCI [1,2]. Spinal cord injuries often result in the loss of motor function, sensory deficits, and can even compromise the health of internal organs, thereby placing substantial economic and psychological burdens on patients and their families.

Despite significant efforts in the medical field, current therapeutic approaches for SCI predominantly include surgical intervention, pharmacological treatments, and rehabilitation strategies. However, these methods have shown limited efficacy in reversing lost neurological functions, and patients often experience only marginal improvements in recovery, with the risk of recurrence persisting [3–6]. Increasingly, research efforts are being directed toward novel strategies for neural regeneration and functional recovery, with electrical stimulation emerging as a particularly promising avenue due to its unique advantages. Studies have demonstrated that electrical stimulation can enhance endogenous neuroplasticity or neuromodulation, thereby retraining or restoring residual neural circuits, offering a new pathway for SCI rehabilitation[7–9]. This technology has already shown considerable potential in the field of spinal cord repair. By promoting the transmission of neural signals, restoring the function of neural pathways, and, under certain conditions, facilitating neuronal regeneration, electrical stimulation offers a promising approach to SCI recovery [10].

Nevertheless, despite its potential, current electrical stimulation devices face multiple challenges in practical application[11]. On one hand, conventional electrical stimulators typically rely on external power sources connected via wires, which not only increase the risk of

* Corresponding authors.
E-mail addresses: zhaowei_2022@163.com (W. Zhao), yj_liu@hit.edu.cn (Y. Liu).

https://doi.org/10.1016/j.nanoen.2025.110895
Received 17 November 2024; Received in revised form 5 March 2025; Accepted 16 March 2025
Available online 20 March 2025

infection but also significantly hinder the patient's daily activities [11–13]. Additionally, most existing implantable stimulators are encased in metallic shells and utilize rigid circuit systems, resulting in large and heavy devices that limit their flexibility during implantation [12,15]. These electrode implants generally exhibit a high elastic modulus in the gigapascal range, rendering them significantly stiffer than the surrounding spinal tissue, which can provoke acute and chronic tissue responses. Over prolonged implantation periods, the mismatch between the stimulator and the biological tissue can lead to local inflammation, reduced cellular activity, and ultimately compromise both the efficacy of the stimulation and the biocompatibility of the device [16].

To address the aforementioned challenges, researchers have developed various flexible electrodes [17–22], which leverage advanced material compositions and structural designs to enhance compatibility and adaptability with biological tissues. For instance, Zhang et al. introduced a stretchable structural design to fabricate a vagus nerve-wrapping electrode inspired by climbing plants. This electrode, utilizing shape-memory polymers, features reconfigurable shapes and tunable elastic moduli, effectively minimizing constraint and damage to the vagus nerve [23]. Additionally, Minev et al. designed a soft neural implant that conforms to the shape and elasticity of the dura mater. The flexible encapsulation, made from functional silicone, significantly reduces compressive damage to the spinal cord due to its excellent tissue compatibility and ultralight structure [24]. Although fully implantable wireless spinal cord stimulators have been realized in previous studies, their large size poses challenges for long-term biocompatibility [25].

Despite the improvements in tissue-electrode interfacing achieved by existing flexible stimulators, they still rely on percutaneous wires, which inevitably increase the risk of infection and displacement. Thus, the development of a novel electrical stimulator capable of overcoming these limitations has become a critical task for researchers. This project proposes a wireless electrical stimulator tailored to the mechanical and geometric characteristics of the spinal cord. It operates through wireless power transmission and exhibits both biocompatibility and implantability. By employing electromagnetic coupling for wireless energy transfer, the stimulator eliminates the need for batteries, resulting in a more lightweight design with external control and programmability, allowing for greater flexibility in application scenarios. Furthermore, by integrating the wireless stimulator with a self-powered spinal motion sensor, we have developed a system capable of both wireless spinal cord stimulation and real-time monitoring of physical health during the treatment process.

This device can be fully implanted within the body, obviating the need for transcutaneous external hardware, thereby minimizing the risk of device-related infection and displacement. This innovative design not only enhances the safety of the stimulator but also improves the convenience for patients in their daily lives. With an optimized micro-geometric design, the electrode structure closely conforms to the spinal tissue, effectively reducing mechanical mismatch and decreasing the likelihood of complications, thus creating more favorable conditions for tissue regeneration. To further enhance the performance of the implanted electrodes, we introduced an inverse structural design. Specifically, this design allows the mechanical modulus of the implanted electrode to closely mimic the non-linear stress-strain behavior of spinal tissue. Compared to most conventional electrodes, this optimized design significantly reduces mechanical mismatch between the implant and the host tissue, thereby minimizing tissue damage and providing a more conducive environment for the normal recovery and regeneration of neural tissues.

In terms of structural design, the electrodes of this wireless stimulator exhibit a high degree of adaptability, allowing them to conform to the spinal tissue of different individuals or regions, ensuring optimal contact with nerves in terms of length, width, and other parameters, thereby greatly enhancing the effectiveness of electrical stimulation. Moreover, the programmable nature of the device allows for the adjustment of stimulation intensity and frequency, enabling patients to tailor the treatment to their specific needs under the guidance of medical professionals.

Furthermore, wireless monitoring of spinal motion is critical for the success of spinal cord stimulation therapy [16,26,27]. Under normal conditions, the mechanical load on the spine is relatively low; however, during high-risk activities (such as severe twisting or heavy lifting), the forces exerted on the spine can increase significantly, potentially leading to damage to the implanted stimulator and secondary spinal injuries [28]. High-risk spinal movements may compromise the integrity of the stimulator, thereby affecting the efficacy of the stimulation therapy. Therefore, monitoring spinal motion is essential for preventing structural damage to the stimulator caused by excessive movements (e.g., increased signal noise in the TENG transmission or altered voltage curves), which plays a crucial role in ensuring the device's long-term integrity[29]. Such monitoring can also help clinicians detect potential electrode displacement early, allowing for timely adjustments.

In addition, spinal motion monitoring is valuable for assessing the patient's functional capabilities in daily life. The flexibility and range of motion of the spine are key indicators of whether a patient is regaining the ability to perform normal daily activities and resume work [30]. By regularly tracking spinal motion, clinicians can offer personalized rehabilitation guidance, helping patients avoid high-risk movements that may lead to new injuries or electrode-related issues. Moreover, as treatment progresses, spinal motion monitoring can assist in evaluating whether the patient's mobility is gradually improving, enabling adjustments to rehabilitation and therapeutic strategies to better support functional recovery. For example, when the TENG (triboelectric nanogenerator) voltage remains below 10 V, it indicates that spinal motion is within a normal range and no intervention is necessary. However, if the voltage exceeds 10 V, it suggests that the range of spinal motion is excessive, posing a risk of secondary injury, and precautions should be taken to prevent such movements (e.g., avoiding severe twisting or heavy lifting).

By designing and developing an integrated system combining a flexible wireless stimulator with a self-powered wireless spinal motion sensor, this study opens new avenues for both treatment and health monitoring of patients with spinal cord injuries. This system not only enhances biocompatibility and flexibility but also effectively reduces the risk of infection and other complications, reflecting the modern trend in medical technology towards personalized, minimally invasive, and efficient therapeutic approaches.

2. Results and discussion

2.1. Design and performance of the wireless electrical stimulator

The proposed system, illustrated in Fig. 1A, integrates wireless spinal cord stimulation and real-time spinal motion monitoring for rehabilitation applications. The wireless radio stimulator receives external electromagnetic energy through a flexible receiving antenna, enabling full-body implantation of the device. Twin-fractal-serpentine-structured electrodes are designed to match the tensile modulus of spinal cord tissue, thereby minimizing mechanical mismatch at the tissue-device interface. Meanwhile, the spinal motion monitor detects and wirelessly transmits kinematic electrical signals via a Bluetooth module to a mobile device for real-time analysis. This integrated system helps prevent high-risk movements during rehabilitation therapy while mitigating secondary injury risks.

Fig. 1B schematically illustrates the composition and integration of the wireless, flexible, and ultrathin neural stimulator with the TENG-based spinal motion monitor. The wireless power harvesting component of the system includes a single-layer inductive coil configuration (molybdenum (Mo); diameter: 35 mm/18 mm; thickness: 50 μm; sourced from Qingyuan Metal Materials Co., Ltd., China), which functions as a loop antenna and is connected in parallel with a flexible

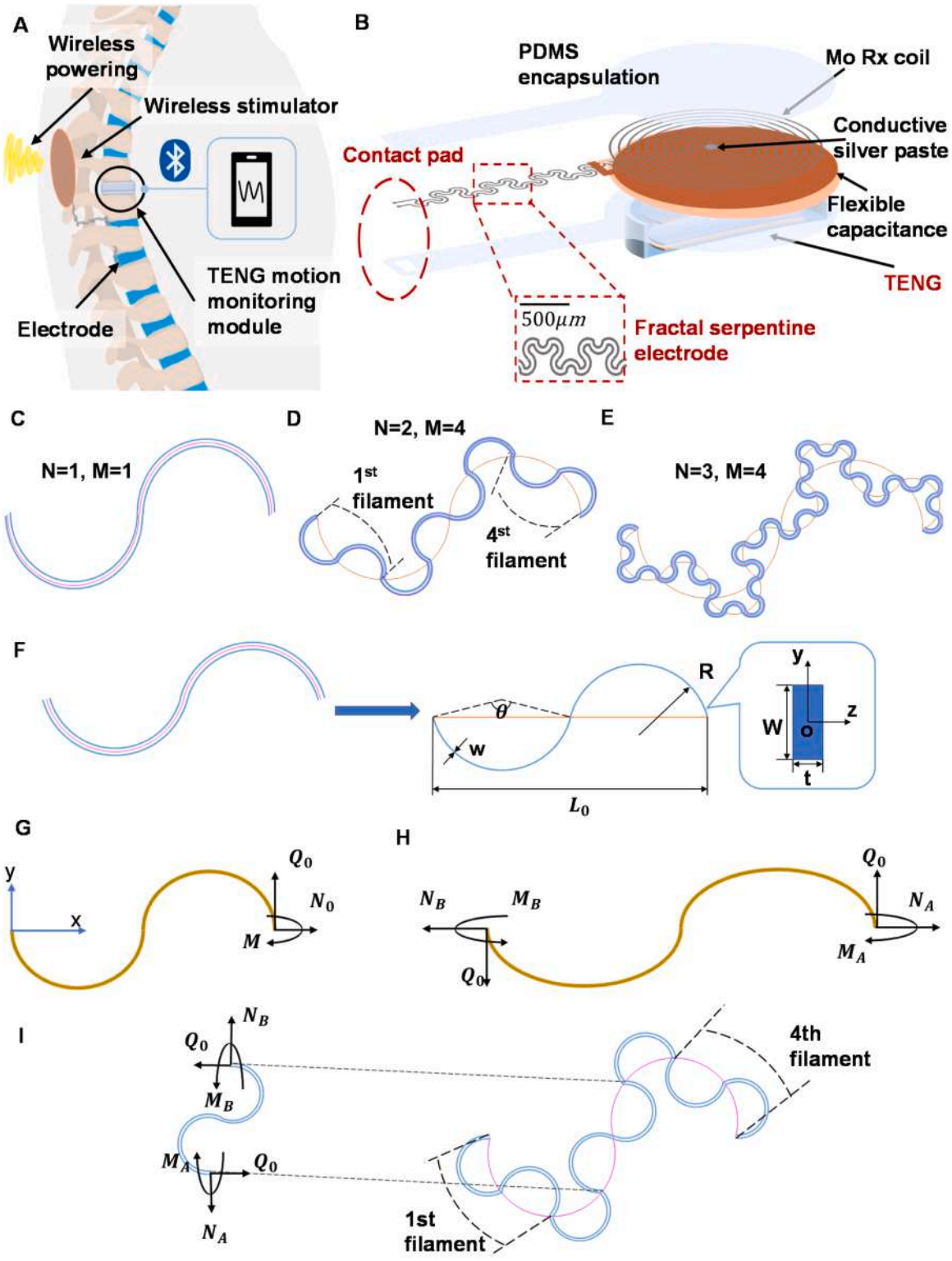

Fig. 1. Design of the wireless electrical stimulator A: Schematic illustration of a system for wireless spinal cord stimulation and spinal motion monitor; B: The structure of the wireless flexible system; C-E: twin serpentine fractal structure design; F: Theoretical analysis model of twin serpentine fractal structure; G-I: Force analysis of twin serpentine fractal structure.

circular capacitor (the complementary structure facilitates the parallel connection). The capacitor utilizes polyimide-coated copper foil (PI-Cu) as the conductor, with DT-15A coating serving as the insulating dielectric layer (thickness: 300 μm; diameter: 35 mm/18 mm), while silver conductive adhesive (04998-AB, SPI, USA) provides electrical interconnections.

The stretchable electrode (Mo; thickness: 50 μm) are designed with a periodic serpentine fractal microstructure, which can be precisely tailored to achieve non-linear mechanical responses in various target tissues, thereby minimizing mechanical mismatch between the implant and host tissue at the implantation site. The inductive coil and serpentine fractal electrodes are fabricated from molybdenum foil via

femtosecond laser processing. Openings at the electrode terminals allow electrical stimulation to be transmitted from the receiver (Rx) antenna to the spinal dura mater.

In addition to mechanical optimization, molybdenum was selected as the electrode material due to its superior ductility, electrical conductivity, and excellent biocompatibility[31,32]. Two layers of polydimethylsiloxane (PDMS) encapsulate the entire system on the top, bottom, and surrounding areas (thickness: 50 μm), ensuring that the active materials are isolated from surrounding biological fluids during implantation. The flexibility of the soft implant allows it to be inserted through a small opening beneath the dura mater. This location provides a close interface between the electrodes and the target neural tissue, enabling more efficient electrical stimulation.

To demonstrate these features, we fabricated an implant tailored to the spinal cord, characterized by its small size, thin profile (receiving antenna (Rx) diameter: 35/18 mm, thickness 700 μm; electrode width: 3 mm, thickness: 150 μm, length can be adjusted as needed.), and lightweight design (0.3 g), suitable for the demanding environment of the central nervous system(Optical picture in Supplementary material 5). We successfully integrated the soft implant into the subdural space of the entire lumbosacral segment, where it conformed to the spinal neural tissue. The implant was securely anchored to the spine using bone screws.

2.1.1. Performance analysis of twin fractal serpentine structure under infinitesimal deformation

The serpentine structure is one of the earliest designs studied in the field of flexible electronics, known for its excellent stretchability and design versatility, making it suitable for various applications. It has been widely adopted in flexible electronic systems [14,18,33]. Inspired by fractal geometry, this project introduces a novel fractal-based, dual-layer serpentine structure. In this design, the structure is subdivided into smaller segments, each replicating the overall geometry in a self-similar manner. The mechanical response of this structure is primarily determined by five geometric parameters: the arc radius (R), arc angle (θ), normalized microstructure width ($\overline{w}$), fractal order (N), and the number of primary units per fractal order (M). Here, the normalized width is defined as $\overline{w} = w/L_0$, where w and L_0 represent the width and effective length of the curved microstructure, respectively (Fig. 1F)[34].

In this study, we establish the load-displacement relationships for the first- and second-order serpentine fractal microstructures based on the assumption of small deformations. Assuming that the structure's thickness (t) is much greater than the width of the ligaments (w), the ligament microstructures are considered to undergo only planar deformation. Since the distance between two serpentine microstructures is much smaller than the arc radius (R), the curves of the two serpentine microstructures can be approximated by the equation of the centerline (the pink dashed line represents the centerline of the two microstructures). We investigate the stress-strain relationship of the single microstructure during the stretching process. The Euler-Bernoulli beam theory is used to simulate its deformation behavior due to the microstructure has an elongated geometry [35].

As shown in Fig. 1G, we use the local Cartesian coordinates to describe the position and geometric parameters of any first-order microstructure and set the left end of the microstructure as the origin. The force applied on the microstructure in the free state is shown in Fig. 1H. The total strain energy of the microstructure can be defined as:

$$U = \frac{1}{2E_S A}\int_0^{S_0} N^2 dS + \frac{1}{2E_S I}\int_0^{S} M^2 dS \tag{1}$$

$$A = wt, I = \frac{w^3 t}{12}, L_0 = 4R_0 \sin\left(\frac{\theta}{2}\right) \tag{2}$$

For the sake of integration, the coordinates of X and $Y$are represented by parametric equations: $X = X(S), Y = Y(S)$, and the curve equation for the microstructure is:

When $S \in [0, \theta R_0]$:

$$\begin{cases} X_{R1} = \dfrac{L_0}{4} \\ Y_{R1} = \dfrac{L_0}{4}\cot\left(\dfrac{\theta}{2}\right) \end{cases} \quad \begin{cases} X(S) = X_{R1} - R\sin\left[\left(\dfrac{\theta}{2}\right) - \dfrac{S}{R}\right] \\ Y(S) = Y_{R1} - R\cos\left[\left(\dfrac{\theta}{2}\right) - \dfrac{S}{R}\right] \end{cases} \tag{3}$$

When $S \in (\theta R_0, 2\theta R_0]$:

$$\begin{cases} X_{R2} = \dfrac{3}{4}L_0 \\ Y_{R2} = -\dfrac{L_0}{4}\cot\left(\dfrac{\theta}{2}\right) \end{cases} \quad \begin{cases} X(S) = X_{R2} - R\sin\left(\dfrac{3}{2}\theta - \dfrac{S}{R}\right) \\ Y(S) = Y_{R2} + R\cos\left(\dfrac{3}{2}\theta - \dfrac{S}{R}\right) \end{cases} \tag{4}$$

The relationship between the tension and torque at each point on the thin line and the force and torque at both ends can be expressed as:

$$\begin{cases} M(S) = M_A + N_0 Y(S) - QX(S) \\ N(S) = N_0 X'(S) + Q_0 Y'(S) \end{cases} \tag{5}$$

By integrating the energy equation we get:

$$U = \frac{1}{2E_S A}\int_0^{S_0} N^2 dS + \frac{1}{2E_S I}\int_0^{S} M^2 dS \tag{6}$$

$$\begin{aligned} U = {} & \frac{L_0}{2E_S A}\left(\beta_1 {N_0}^2 + \beta_2 N_0 \frac{M_A - M_B}{L_0} + \beta_3 \frac{{M_A}^2 + {M_B}^2 - 2M_A M_B}{{L_0}^2}\right) \\ & + \frac{L_0}{2E_S I}\Big[\beta_4 {M_4}^2 + \beta_5 (N_0 L_0)^2 + \beta_6 \left({M_A}^2 + {M_B}^2 - 2M_A M_B\right) \\ & + \beta_7 M_A (N_0 L_0) + \beta_8 M_A (M_A - M_B) + \beta_9 (N_0 L_0)(M_A - M_B)\Big] \end{aligned} \tag{7}$$

where $\beta_1 = \frac{1}{L_0}\int_0^{S_0} [X]^2 dS = \frac{1}{4}\left(\csc\frac{\theta}{2}\right)(\sin\theta + \theta)$, $\beta_2 = \frac{2}{{L_0}^2}\int_0^{S_0} X'Y' dS = 0$, $\beta_3 = \frac{1}{L_0}\int_0^{S_0} [Y]^2 dS = \left(\csc\frac{\theta}{2}\right)\frac{(\theta - \sin\theta)}{4}$, $\beta_4 = \frac{S_0}{L_0} = \frac{\theta}{2}\csc\frac{\theta}{2}$, $\beta_5 = \frac{1}{{L_0}^3}\int_0^{S_0} [Y(S)]^2 dS = \csc\frac{\theta}{2}\frac{\left[\csc^2\frac{\theta}{2}(\theta + \sin\theta) + 2\cot^2\frac{\theta}{2} - 4\sin\theta\right]}{64}$, $\beta_6 = \frac{1}{{L_0}^3}\int_0^{S_0} [X(S)]^2 dS = \csc\frac{\theta}{2}\frac{\left(10\theta + \theta\csc^2\frac{\theta}{2} - \csc\frac{\theta}{2}\right)}{64}$, $\beta_7 = \frac{2}{L_0}\int_0^{S_0} Y(S) dS = 0$, $\beta_8 = -\frac{2}{L_0}\int_0^{S_0} X(S) dS = -\frac{\theta}{2}\csc\frac{\theta}{2}$, $\beta_9 = -\frac{2}{{L_0}^2}\int_0^{S_0} X(S)Y(S) dS = \frac{\left(\theta\cos\frac{\theta}{2} - 2\csc\frac{\theta}{2}\right)}{16}$.

Here, S_0 represents the total length of the microstructure and E_S represents the elastic modulus of the constituent material. According to Castiglione's theorem, the load-displacement equation can be written in dimensionless form as follows:

$$\begin{Bmatrix} \overline{u} \\ w_A \\ w_B \end{Bmatrix} = \begin{bmatrix} \frac{\overline{w}^2\beta_1}{12} + \beta_5 & \frac{\overline{w}^2\beta_2}{24} + \frac{1}{2}\beta_7 + \frac{1}{2}\beta_9 & -\frac{\overline{w}^2\beta_2}{24} - \frac{1}{2}\beta_9 \\ \frac{\overline{w}^2\beta_2}{24} + \frac{1}{2}\beta_7 + \frac{1}{2}\beta_9 & \frac{\overline{w}^2\beta_3}{12} + \beta_4 + \beta_6 + \beta_8 & -\frac{\overline{w}^2\beta_3}{12} - \beta_6 - \frac{1}{2}\beta_8 \\ -\frac{\overline{w}^2\beta_2}{24} - \frac{1}{2}\beta_9 & -\frac{\overline{w}^2\beta_3}{12} - \beta_6 - \frac{1}{2}\beta_8 & \frac{\overline{w}^2\beta_3}{12} + \beta_6 \end{bmatrix} \begin{Bmatrix} \overline{N}_0 \\ \overline{M}_A \\ \overline{M}_B \end{Bmatrix} \tag{8}$$

$$\overline{u} = \frac{u}{L_0}, \overline{w} = \frac{w}{L_0}, \overline{N}_0 = \frac{N_0 {L_0}^2}{E_S I}, \overline{Q}_0 = \frac{Q_0 {L_0}^2}{E_S I}, \overline{M}_A = \frac{M_A L_0}{E_S I}, \overline{M}_B = \frac{M_B L_0}{E_S I} \tag{9}$$

To find the equivalent tensile stiffness of the structural element, we assume that the serpentine element is only subjected to tension. The relationship between the strain and the normalized external force of the structural element is:

$$\varepsilon_X = \overline{u} = \left(\frac{\overline{w}\beta_1}{12} + \beta_5\right)\overline{N}_0 \tag{10}$$

The projection of the thin line in the y direction is taken as the

equivalent width, multiplied by the thickness to obtain the equivalent area of the unit$S = 4R_0\left[1 + \cos\left(\pi - \frac{\theta}{2}\right)\right]t$, and the tension is divided by the equivalent area to obtain the unit equivalent stress:

$$\delta_X = \frac{N_0}{4R_0\left[1 + \cos\left(\pi - \frac{\theta}{2}\right)\right]t} \tag{11}$$

The force on the two microstructures is approximately δ_X, and the direction is the negative direction of the x-axis. The stress of the twin serpentine structure is $2\delta_X$, and the strain is ε_X. The ratio of the equivalent tensile stiffness of the twin serpentine unit to the tensile stiffness can be expressed as:

$$\overline{E} = \frac{E_X}{E_S} = \frac{2\delta_X}{\varepsilon_X E_S} = \frac{\overline{w}^3 \sin\left(\frac{\theta}{2}\right)}{6\left[1 - \cos\left(\frac{\theta}{2}\right)\right]\left(\frac{\overline{w}}{12}\beta_1 + \beta_5\right)} \tag{12}$$

Similarly, for the second-order fractal structure, we only need to calculate β_1 and β_5 by integrating the energy equation and then substitute them into the above formula to get its dimensionless tensile stiffness ratio $\overline{E}$. It is only determined by the dimensionless width ($\overline{w}$) and the radian (θ)(Supplementary material 2).

2.1.2. *Performance analysis of twin fractal serpentine structure under finite deformation*

To validate the mechanical behavior of the twin fractal serpentine structure under finite deformation, we conducted a series of simulations in the finite element software ABAQUS under uniaxial tension (Supplementary material 3), with a material Young's modulus of 324 GPa and a Poisson's ratio of 0.3 [31,32,36]. A set of structures with different design parameters of *N*, *M*, θ, and normalized width ($\overline{w}$) were designed to investigate the influence on the mechanical properties.

Fig. 2 presents the equivalent tensile stiffness ratio E^*/E_s (equivalent tensile stiffness E^*, elastic modulus of the constituent material: E_S) of the twin fractal serpentine structure, which is defined as the ratio of the force applied to one end of the structure (while the other end is fixed) to the equivalent area. The results of the analytical model are represented by curves, while the finite element method (FEM) results are depicted as discrete points. It indicates that the FEM data align well with the analytical solution in Fig. 2, demonstrating that the energy-based method provides a reasonably accurate prediction of the global load-displacement behavior.

As shown in Fig. 2A-D, the effects of both variables on the equivalent tensile stiffness ratio are monotonic: a smaller θ and a larger $\overline{w}$ lead to a lower equivalent stiffness ratio. It can be seen that by altering the design parameters, the stiffness of the system can be reduced by several orders of magnitude. This mechanism enables the fabrication of tissue-like soft electronics using serpentine rigid materials such as silicon and gold [37–39].

To further explain the influence of θ and $\overline{w}$ on the mechanical properties, the contour plots are employed to illustrate the normalized equivalent stiffness ratio. Fig. 3 presents these contour plots for various configurations: Fig. 3A for (N = 1), Fig. 3B for (N = 2, M = 2), Fig. 3C for (N = 2, M = 3), and Fig. 3D for (N = 2, M = 4). The color scale represents the base-10 logarithm of the equivalent tensile stiffness ratio(E^*/E_S). The conclusions drawn from these contour plots are consistent with the observations from the graphs.

The FEA results of the stress-strain ($\delta - \varepsilon$) curve in the x-direction with a width of $\overline{w}$= 0.025 are shown in Fig. 4. As illustrated in Fig. 4A and F, the structures gradually straighten as ε increases. Fig. 4B-E present the experimental $\delta - \varepsilon$ curves for the structures with the design of first-order fractal geometry. As shown in the figure, The process is mainly divided into two stages, the first stage is the process of gradually straightening the structure from the bending state, and the second stage is the stage of elastic deformation or plastic deformation of the structure. Due to the different deformation modes of the two stages, the equivalent elastic modulus of the two stages will be quite different, and the stress-strain curve will further show a J-shaped $\delta - \varepsilon$ curve (Supplementary

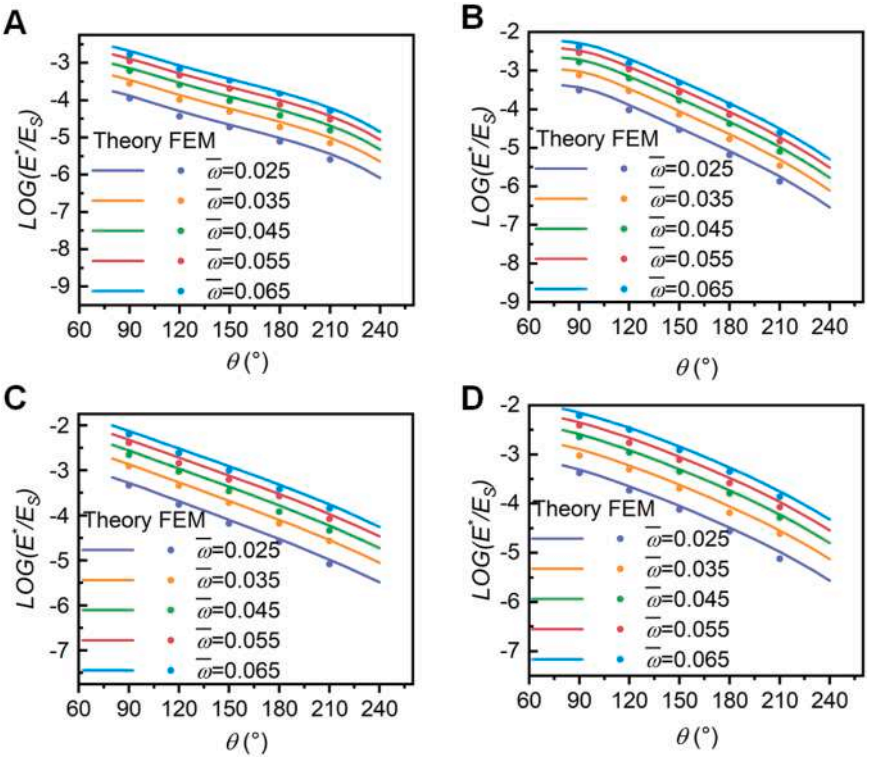

Fig. 2. Theoretical and finite element analysis results of equivalent tensile stiffness ratio of twin fractal serpentine structures with different geometric parameters: A: N = 1, B: N = 2 and M= 2, C: N = 2 and M= 3, D: N = 2 and M= 4.

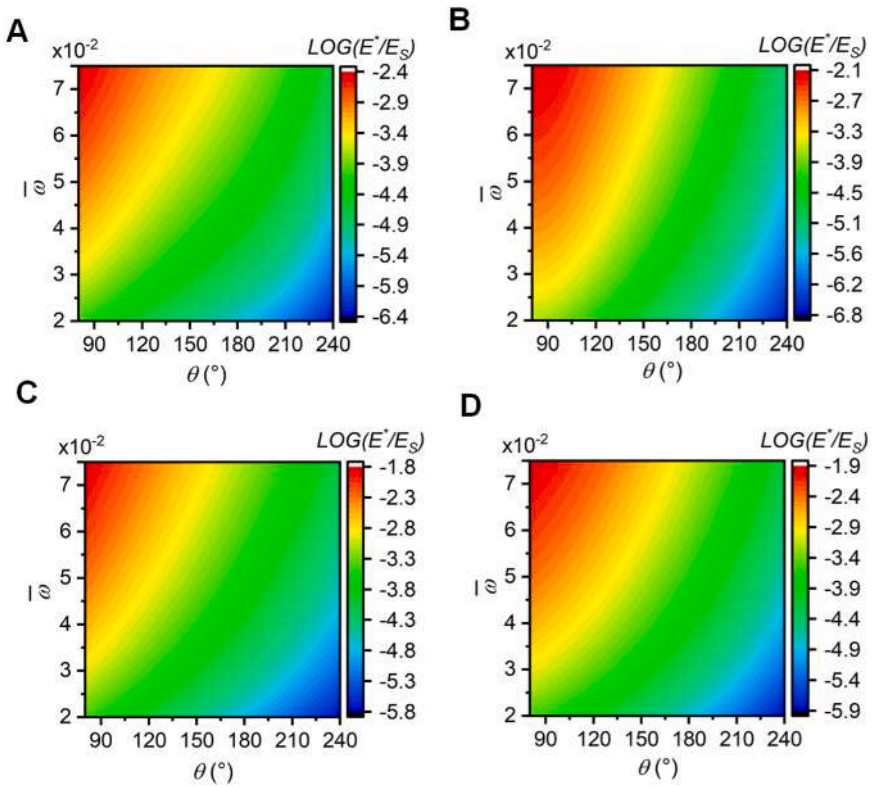

Fig. 3. Theoretical cloud diagram of equivalent tensile stiffness of twin fractal serpentine structure with different geometric parameters A: N = 1, B: N = 2 and M= 2, C: N = 2 and M= 3, D: N = 2 and M= 4.

Video 1). Initially, the structure experiences a bending-dominated phase at low strains, during which the curved microstructure gradually unfolds as ε increases. In this first phase, the $\delta-\varepsilon$ curve exhibits relatively modest growth with increasing strain, indicative of a low effective tensile stiffness. As the bent microstructure is stretched to a nearly straight configuration, a distinct phase of rapid growth in the stress-strain curve emerges with further increases in strain. Subsequently, the serpentine structure transitions into a tension-dominated deformation phase (the second phase), during which the microstructure is fully stretched into a linear configuration. This transition is completed once the bending components are fully straightened, and the J-shaped $\delta-\varepsilon$ curve enters a linear hardening regime, characterized by rapid growth in stress and a significantly higher effective elastic modulus. Furthermore, the results indicated that the equivalent tensile stiffness ratio (E^*/E_S) decreases with increasing θ.

Fig. 4G presents the FEA results for tension in the x-direction for models with different values of N, M, ($\overline{w} = 0.025, \theta = 210°$). The results indicate that, as the fractal order N increases, the maximum strain of the structure increases, the tensile performance is enhanced, and the equivalent stiffness ratio decreases. A comparison between the curves for $M = 2$ and $M = 4$ reveals that, with an increase in the number of microstructural repetitions (M), the equivalent stiffness ratio increases during the linear regime of the first phase. However, in the nonlinear regime of the second phase, the maximum tensile strain of the structure increases. Fig. 4IJ shows the stress distribution in the structures after FEA stretching. It can be seen that the stress is mainly concentrated in the top and bottom arcs.

Fig. 4H compares the mechanical properties of second-order fractal serpentine structures ($\theta = 210°$, (N = 2), (M = 2), (M = 3), and (M = 4)) with the stress-strain curve for porcine spinal cord under uniaxial tension[40,41]. The uniaxial tensile stress-strain curves of the twin fractal serpentine structures exhibit a certain degree of fit with the porcine spinal cord's J curve. Specifically, the ($N = 2$, $M = 4$) structure, shows a high degree of matching with the porcine spinal cord curve in the strain range from $\varepsilon = 0.5$ to $\varepsilon = 0.7$. By adjusting design parameters such as N, M, θ, and $\overline{w}$, the mechanical properties can be tailored to suit various application scenarios. In the electrode stretching experiment, we connect the encapsulated electrode in series with 24 light-emitting diodes (LEDs) (1.5 V, Shenzhen Hongtu Weiye Components Mall) and apply a 36 V DC voltage across both ends. As a result, all LEDs work normally; when the electrode is stretched to a strain of 70 %, the LEDs' brightness dose not change (Supplementary Video 2). As shown in the Supplementary Material 4, we measured the resistance of the twin fractal serpentine electrodes during the stretching process and observed that the variation in resistance was minimal relative to the applied load (with a cortical resistance of 27 Ω/mm)[42]. This finding demonstrates the favorable electrical properties of this structure for neural electrical stimulation.

2.1.3. Analysis of wireless radio stimulation performance

2.1.3.1. Wireless stimulator preparation process. Fig. 5A illustrates the fabrication process of the flexible wireless spinal cord stimulator. The flexible capacitor is composed of a flexible polyimide copper-clad foil (ASC-FC015SIT1, PI-Coverlay, thickness: 250 μm, provided by Zhongshan Xinhao Electronic Materials Co., Ltd.) and a dielectric coating (LOGI-DT15A, supplied by Shanghai Mifang Technology Co., Ltd., thickness: 50 μm). Two sections of the polyimide copper-clad foil are left uncovered by the dielectric material on the tail ends, forming oppositely oriented L-shaped regions of differing sizes for electrical connections. The L-shaped conductive portion of copper conductor 1 faces downward, while that of copper-clad foil 2 faces upward(Optical picture in Supplementary material 5).

During the assembly of the capacitor and inductor coil, electrode wire 1 is threaded through the L-shaped section of conductor 2 from below and electrically connected to the L-shaped conductive region of conductor 1. Electrode wire 2 is placed on top of the assembly and electrically connected to the L-shaped conductive region of conductor 2

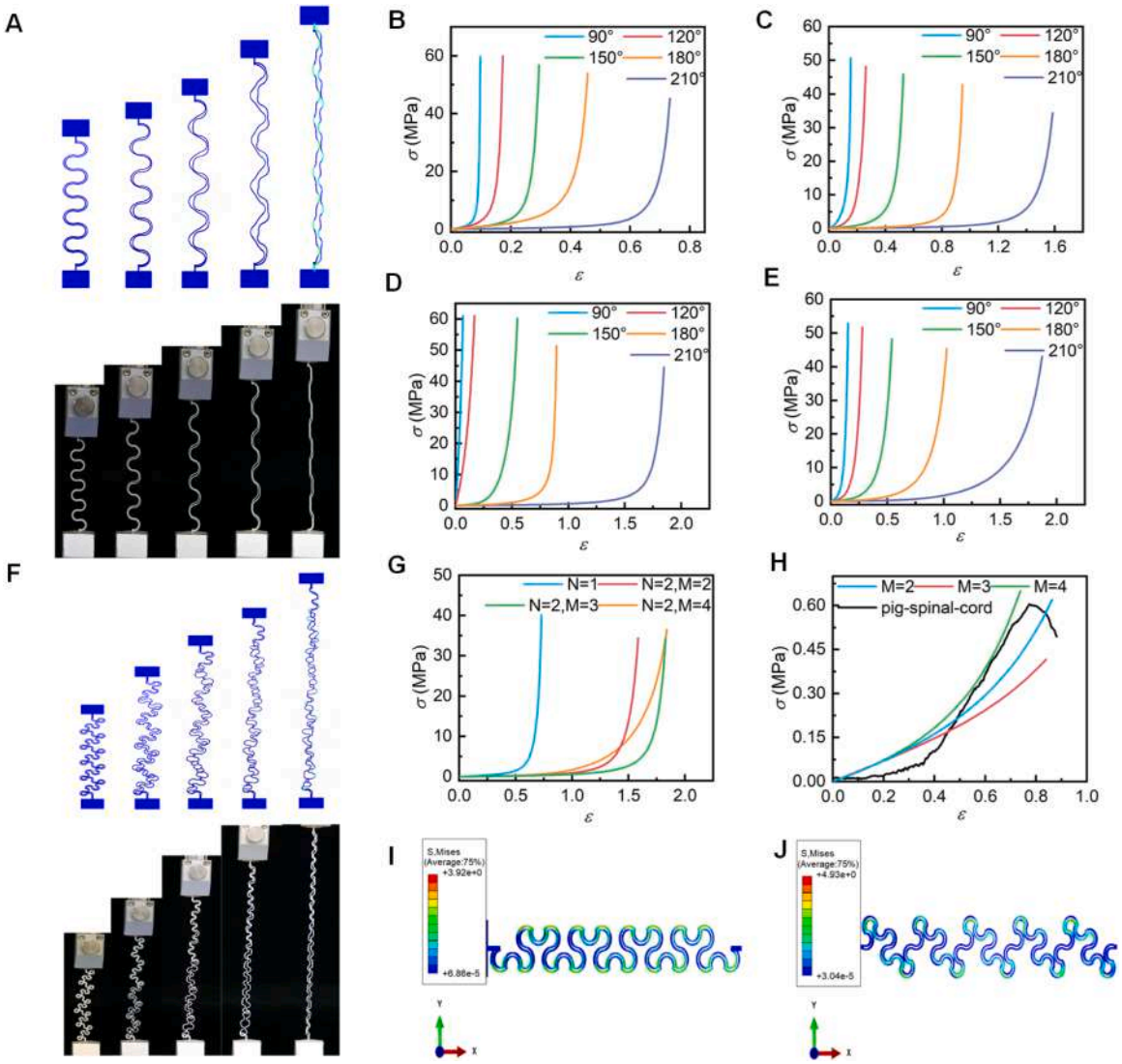

Fig. 4. Experimental and FEA results of twin fractal serpentine structure stretching$\sigma-\varepsilon$ A: Comparison of FEA and experiment of first-order (N = 1) twin fractal serpentine structure under stretching; B-E: Longitudinal stretching results of twin fractal serpentine structure under different fractal parameters (N = 1, N = 2 M=2; N = 2 M=3; N = 2 M=4); G: Comparison of stress-strain curves of twin fractal serpentine structure with different fractal parameters, (θ = 210°, N = 1, N = 2 M=2, N = 2 M=3, N = 2 M=4); H: Comparison of stress-strain curves of twin fractal serpentine structure with different fractal parameters (second-order (N = 2) M= 2, M= 3, M= 4 structures) under small deformation and stress-strain curves of porcine spinal cord, θ = 210°; I-J: stress distribution diagrams of FEA analysis results of (N = 2, θ = 210°) M= 3 and M= 4, respectively. F: Comparison of FEA and experiment of second-order (N = 2, M=4) twin fractal serpentine structure under stretching.

using silver conductive adhesive (04998-AB, SPI Supplies, USA). Finally, the entire system is encapsulated within two layers of PDMS (50 μm, Dongguan Jieli New Materials Co., Ltd.) membranes with a thickness of 50 μm. The dimensions of the device are as follows: receiving antenna (Rx) diameter: 35/18 mm, thickness 700 μm; electrode width: 3 mm, thickness: 150 μm, length can be adjusted as needed.

2.1.3.2. Electrical performance characterization. To guide in vivo experiments, we conducted ex vivo tests to evaluate the wireless transmission capability of the electrical stimulator (electrical measuring equipment in Supplementary material 6). A square wave signal was transmitted from the input antenna (Tx; OK 30# wire, diameter 35 mm, 200 turns) to the output antenna. The square wave signal was generated using a DC power supply (UNI-T UTP3315TFL) and an inverter (DC-AC module; 4–30 V; Foshan Nanhai Fengluan Electrical Co., Ltd.), with the logic circuit shown in Fig. 5B. The power transmission efficiency of the device depends on the mutual inductance between the Rx and Tx coils. This relationship is expressed as $M = \sqrt{L_{Tx}L_{Rx}}$, where L_{Tx} and L_{Rx} represent the inductance of the individual coils, and the coupling coefficient (k) defines the degree of magnetic flux linkage; its value primarily depends on the distance and relative orientation between the coils[43,44]. Proper design choices ensure that the average distance between the skin and spinal cord in adult patients (lumbosacral region, 10 ± 3 mm) is accommodated [45]. Fig. 5C shows the relationship between input and output voltages for two different-sized receiving antennas at a Tx-Rx distance of 2 mm. The antenna with a diameter of 35 mm demonstrates a favorable input-output voltage relationship, achieving an output voltage of 2.5 V when the input voltage is 15 V. Fig. 5D illustrates the relationship between output voltage and the distance between the input and output coils, with an input voltage of 12 V. At a transmission distance of 10 mm, the larger coil (D = 35 mm) still maintains an output voltage of 0.8 V, which meets the requirements for spinal cord stimulation in rats [46].

2.1.3.3. In vivo spinal cord stimulation experiments. We conducted in vivo wireless spinal cord stimulation experiments on a rat model (three

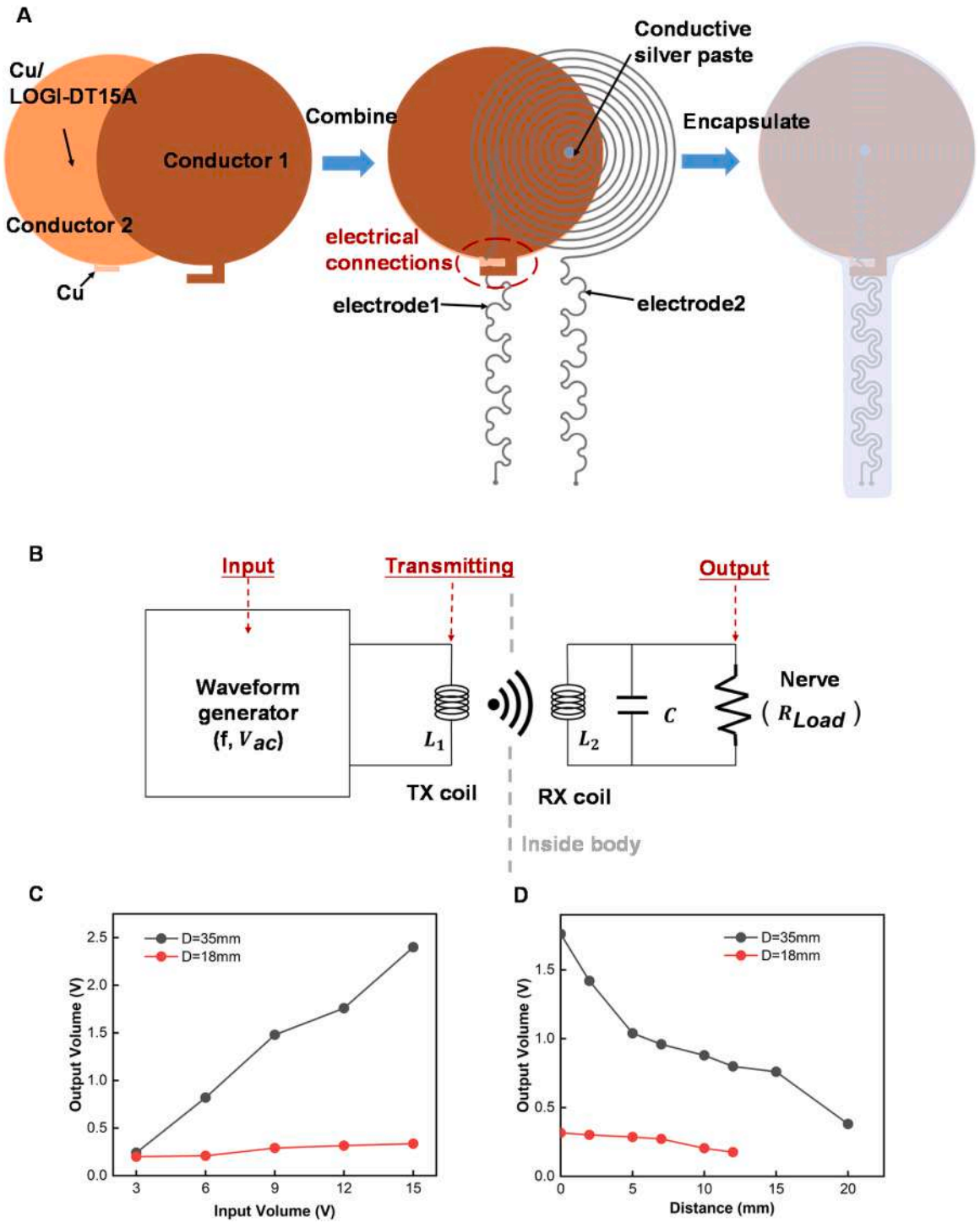

Fig. 5. Preparation process and performance characterization of spinal cord nerve stimulator; A: Schematic diagram of the preparation process of the flexible wireless spinal cord nerve stimulator; B: Electrical stimulation logic circuit diagram; C: Relationship between voltage input and output of antennas with different diameters; D: Relationship between output voltage and transmission distance of antennas with different diameters (input voltage is 12 V).

male rats, 350g-400g, implanted with a stimulator antenna of 35 mm diameter) to demonstrate the practical biomedical significance of the wireless stimulator and to measure electroencephalographic (EEG) responses (Fig. 6). Fig. 6A provides a schematic of the spinal cord stimulation experiment, while Fig. 6B-C show the implantation sites of the spinal cord stimulation electrodes. Fig. 6D depicts the implantation process of the spinal cord stimulator. The electrode was inserted into the epidural space through a partial laminectomy between T11 and T12, and positioned at the L1 and L2 vertebral levels to cover the caudal region of the lumbar spinal cord. The receiving coil (Rx) was placed between the dorsal muscles and skin, centered along the spine. EEG recordings were obtained using a commercial system (Digital Lynx SX - Neuralynx), with microelectrode arrays (Neuronexus, Jiangsu Brain-Machine Technology Co., Ltd.) used as the recording electrodes. The detection electrodes were surgically implanted into the primary motor cortex of the rat brain at a depth of 1.5 mm and secured with medical bone cement[47].

The implementation of electrical stimulation relies on an external

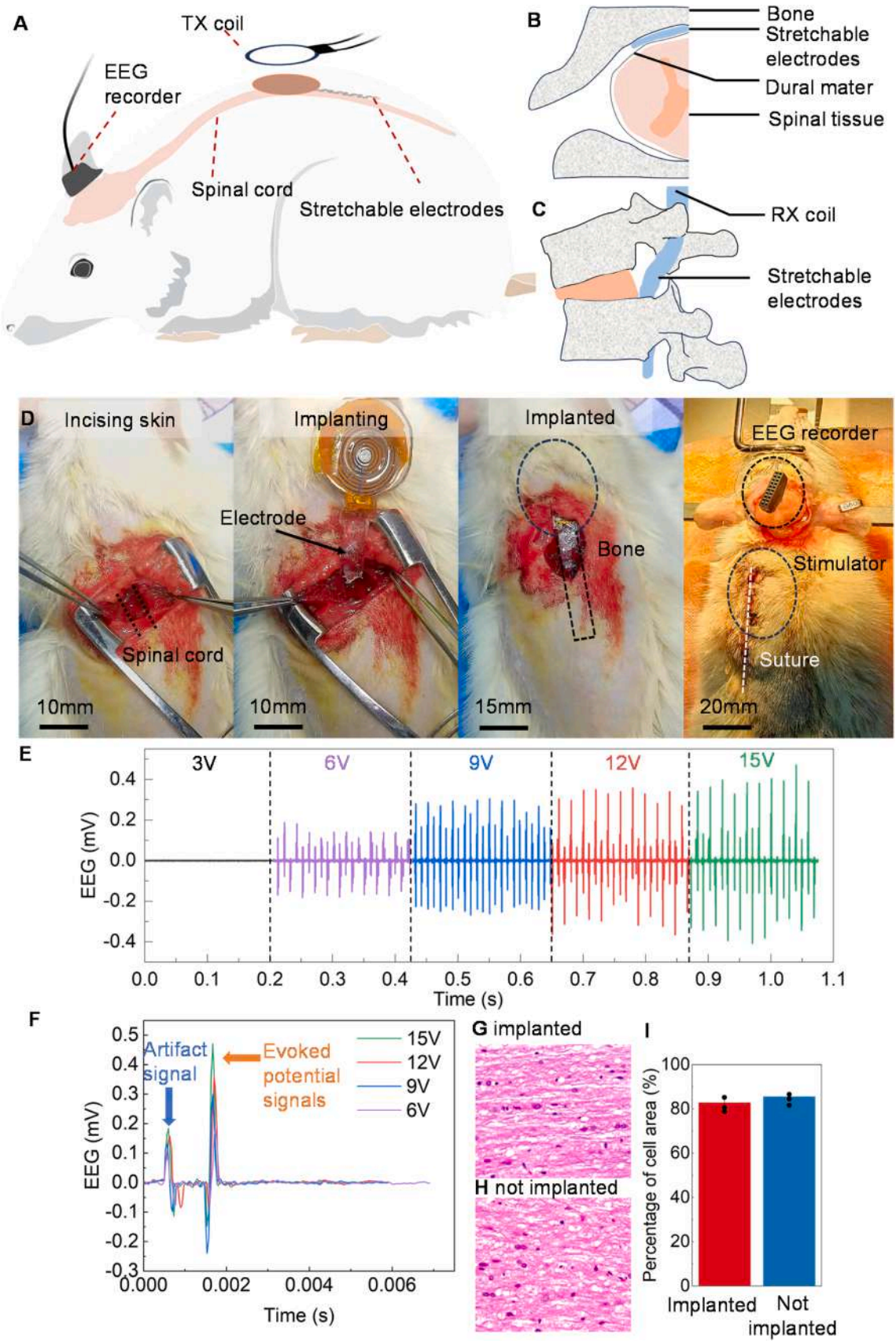

Fig. 6. Experimental surgery of spinal cord stimulation; A: Schematic diagram of spinal cord stimulation experiment; B-C: Front view and side view of the implantation position of the electrical stimulation electrode; D: Optical image of the implantation surgery of the flexible wireless spinal cord stimulator; E: EEG signal image of the electrical stimulation experiment; F: EEG response waveform at different voltages; GHI: blind pathological analysis results after 21 days;GH: Comparison of HE staining results; I: is the cell survival rate.

input coil, the Tx antenna (OK30 #wire, 35 mm in diameter, 100 turns), positioned 2 mm from the surface of the rat's body and oriented perpendicularly to the receiving coil of the spinal cord stimulator. Upon energization, the antenna supplies power to the implanted device. During testing, the rats were anesthetized, and square-wave electrical signals with voltages of 3 V, 6 V, 9 V, 12 V, and 15 V, a pulse width of 10 microseconds, and a frequency of 50 Hz were sequentially applied to the Tx antenna. Simultaneously, changes in the rats' electroencephalogram (EEG) signals were recorded. As shown in Fig. 6E, the evoked EEG action potentials(EEGAPs) recorded from the first motor cortical area of the cerebral cortex were captured. All recorded signals exhibited stimulation artifacts followed by evoked EEGAPs. The amplitude and waveform of the evoked EEGAPs remained nearly constant across each stimulation event[48]. An enlarged comparison of four evoked EEGAPs is presented in Fig. 6F. While the waveforms were consistent, the peak potentials (i.e., 189, 299, 359, and 417 μV) increased proportionally with the applied voltage to the Tx antenna, which is consistent with previously reported literature [49,50]. This demonstrates that the spinal cord neurostimulator is capable of meeting the therapeutic requirements for spinal cord stimulation, providing a viable solution for the development of the next generation of flexible wireless neurostimulators.

To evaluate the biocompatibility of the neurostimulator with biological tissues, we assessed the in vivo biocompatibility of the electrode-spinal cord interface in a dorsal subcutaneous implantation rat model after 21 days (Fig. 6G-H-I). Blinded histopathological evaluations of the tissue revealed comparable tissue responses between the implanted and non-implanted spinal cord sections after 21 days, with no significant inflammatory response observed following the implantation of the neurostimulation device (P = 0.27, Fig. 6I)[51].

2.2. Design and characterization of TENG-based spinal motion monitor

2.2.1. TENG electrical output performance

The functionality of the triboelectric nanogenerator (TENG) is based on the principles of triboelectric effects and electrostatic induction, which take place when two materials make contact and subsequently separate. In the contact-separation mode, the TENG employs two triboelectric materials, with appropriate electrode connections and insulation between the various layers. This study presents a configuration that includes a metal (Cu, Diameter: 40 mm; thickness: 65 μm) paired with a dielectric (PTFE, Diameter: 40 mm; thickness: 100 μm), encapsulated by two thin PDMS film (thickness: 50 μm) (refer to Fig. 7A). When mechanical forces—such as pressure, bending, or vibration—are exerted on the TENG, the two triboelectric layers make contact and then part. This movement disrupts the electrostatic equilibrium, generating a potential difference across the electrodes. Ongoing mechanical actions in both forward and reverse directions induce alternating positive and negative potentials between the triboelectric layers, facilitating charge generation, as depicted in Fig. 7B. The electrodes capture these charges, which can then be harnessed as a source of energy [52,53]. The internal structure of the TENG, as well as its integration into the overall neurostimulator system, is depicted in Fig. 7A. Here, PETF serves as the triboelectric negative layer, with a Cu slice functioning as both the electrode and the second triboelectric material. The entire TENG is circular in shape and forms concentric rings with the electromagnetic induction coil described in Section 4.1.

The electrical output properties of the triboelectric nanogenerator (TENG) were quantitatively tested(electrical measuring equipment in Supplementary material 6), as depicted in Fig. 7C–K. A 15 cm × 15 cm nylon plate, driven by a linear motor (LPS1, China), was used to cyclically apply force to the TENG sample. From the data presented in Fig. 7, we investigated the influence of the applied force and the gap between the TENG layers on its electrical output. When the cycling frequency was fixed at 1 Hz (Fig. 7C–E), the short-circuit transferred charge (Q_{SC}) increased from 2.12 nC to 3.40 nC as the applied force rose from 10 N to 90 N. This phenomenon is attributed to the fact that a larger force generates a greater contact area, thereby enhancing the triboelectric charge transfer. It indicates that the device efficiently converts increased mechanical energy into electrical energy as the applied force intensifies. Since the open-circuit voltage (V_{OC}) and maximum short-circuit current (I_{SC}) are dependent on the amount of transferred charge, they also increased with force, rising from 6.96 V and 34.68 nA to 11.96 V and 152.91 nA, respectively.

When the applied force was fixed at 70 N (Fig. 7F), both *Qsc* and *Voc* remained relatively stable at approximately 3.35 nC and 10.59 V. Furthermore, when the applied force was held constant at 50 N, and the gap distance between the TENG layers was varied (Fig. 7G–H), the values of *Voc*, *Isc*, and *Qsc* exhibited a slight increase as the gap increased from 2 mm to 8 mm (from 8.74 V to 9.48 V, 123.00 nA to 162.71 nA, and 3.03 nC to 3.23 nC, respectively). The maximum output values of 9.48 V, 123.00 nA, and 3.23 nC were recorded at a gap of 8 mm.

The TENG demonstrated good pressure sensitivity (Fig. 7J), with a sensitivity of 0.082 mV/Pa in the range of 0–40 kPa. Furthermore, the output voltage, output current, and power density (*P*) of the TENG were evaluated as functions of varying load resistance (from 10^4 to 10^{10} Ω). Power density was calculated using the formula: $P = I^2/R$, where-*I*denotes the output current, *R* represents the load resistance, and *A* indicates the contact area of the TENG[54]. As shown in Fig. 7I, the maximum power output of 740 μW/m^2 was achieved at a load resistance of 60 MΩ. Additionally, the TENG exhibited consistent pressure sensitivity across specific pressure ranges, making it suitable for potential applications in spinal motion sensing. A fitting analysis (Fig. 7J) yielded a pressure sensitivity of 0.082 mV/Pa within the 0–40 kPa range, ensuring robust performance for future applications in spinal motion sensing. To assess the durability of the TENG, we conducted 2000 cycles of repetitive testing. The results (Fig. 7K) showed no significant variation in V_{OC}, which remained stable at approximately 12 V, with the cycling frequency fixed at 1 Hz. This demonstrates the long-term reliability of the TENG under continuous operation.

2.2.2. Function verification of the TENG-based spinal motion monitor

As illustrated in Fig. 8A, a spinal motion monitor integrating a TENG and a wireless transmitter was developed. The TENG was implanted in the intervertebral disc region of a human spinal model to record the electrical signals generated by spinal movement. These signals were wirelessly transmitted via Bluetooth to a mobile device for real-time analysis. In this study, a spinal model was used to simulate three types of human activities: bending, walking, and jogging (Fig. 8B, Supplementary Video 3). The electrical signals generated by the TENG under these conditions were measured. The results demonstrated that the voltage output of the TENG was triggered by spinal motion. The periodic compression and separation between the vertebrae induced contact and separation of the TENG's triboelectric layers, resulting in electrical output.

The wirelessly transmitted signals revealed that the electrical output from the TENG increased with the intensity of the movement. During the spinal model simulation of bending (Fig. 8C), the output voltage was the smallest (mean: 19 mV; peak: −44 mV). During the walking simulation (Fig. 8D), the output voltage was higher (mean: 38 mV; peak: −53 mV). The highest output voltage was observed during the jogging simulation (Fig. 8E), with a mean of 49 mV and a peak of −60 mV. Furthermore, the frequency and waveform of the signals varied across different movement patterns, providing a theoretical foundation for motion detection and stimulator status monitoring.

Overall, these results indicate that the TENG functions as an effective energy harvester, capable of converting biomechanical energy from spinal movements into electrical signals. The compression and release activities between the vertebrae cause the periodic separation and contact of the two triboelectric layers in the TENG, enabling it to serve as a sensor for monitoring spinal activity. Additionally, the TENG is sensitive to pressure changes between the vertebrae. During hazardous movements, increased pressure leads to a significant rise in the TENG's

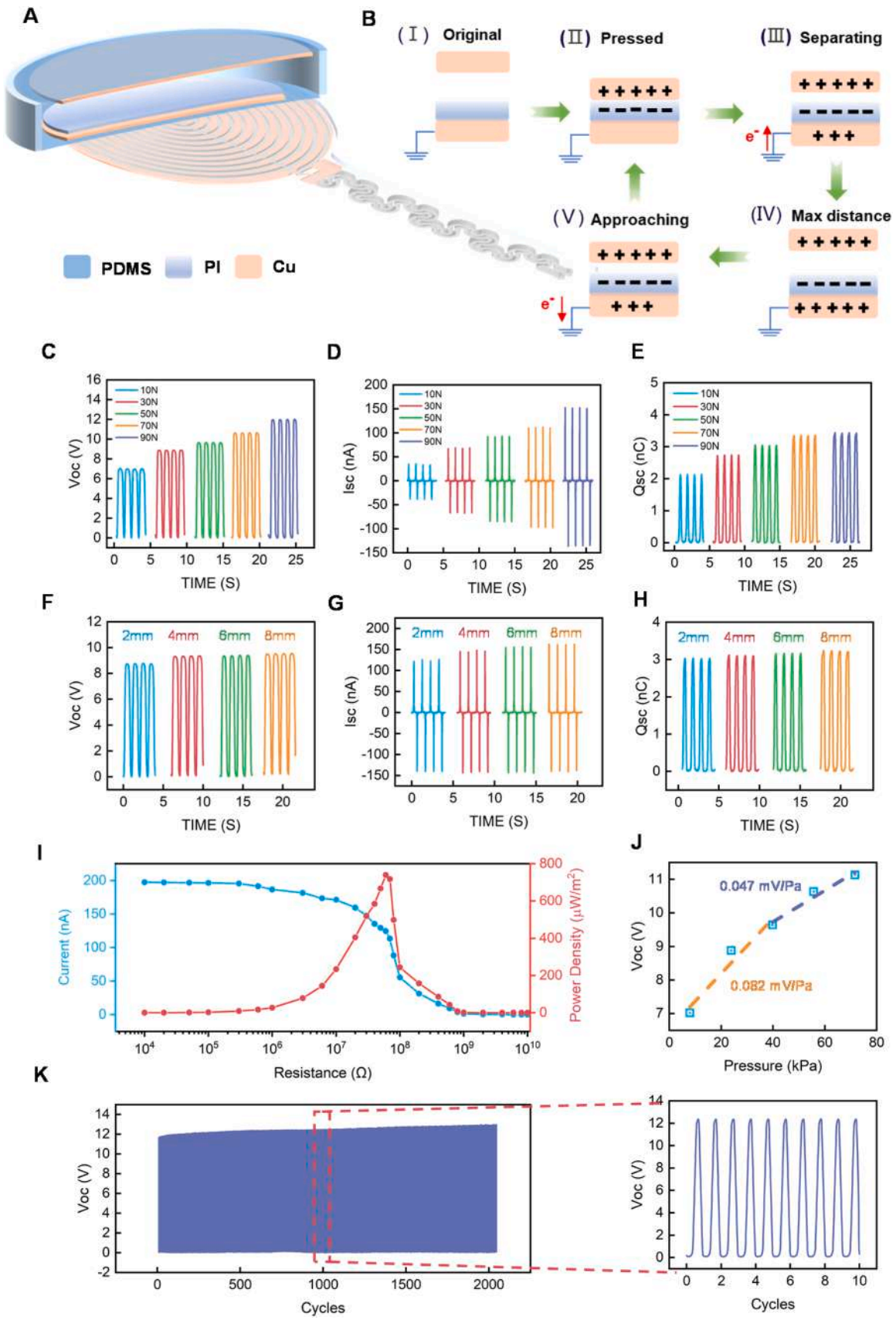

Fig. 7. A: TENG spinal motion monitor structure and electrical stimulator integration; B: Fundamental working modes; C-E: Open circuit voltage (*Voc*), short circuit current (*Isc*) and charge transfer (*Qsc*) of TENG under various applied force (10–90 N); F-H: Open circuit voltage (*Voc*), short circuit current (*Isc*) and charge transfer (*Qsc*) of TENG under different gaps (2–8 mm); I: *Voc* and power density as a function of varying load resistance; J: Linear fitting between *Voc* and applied force; K: Fatigue testing result.

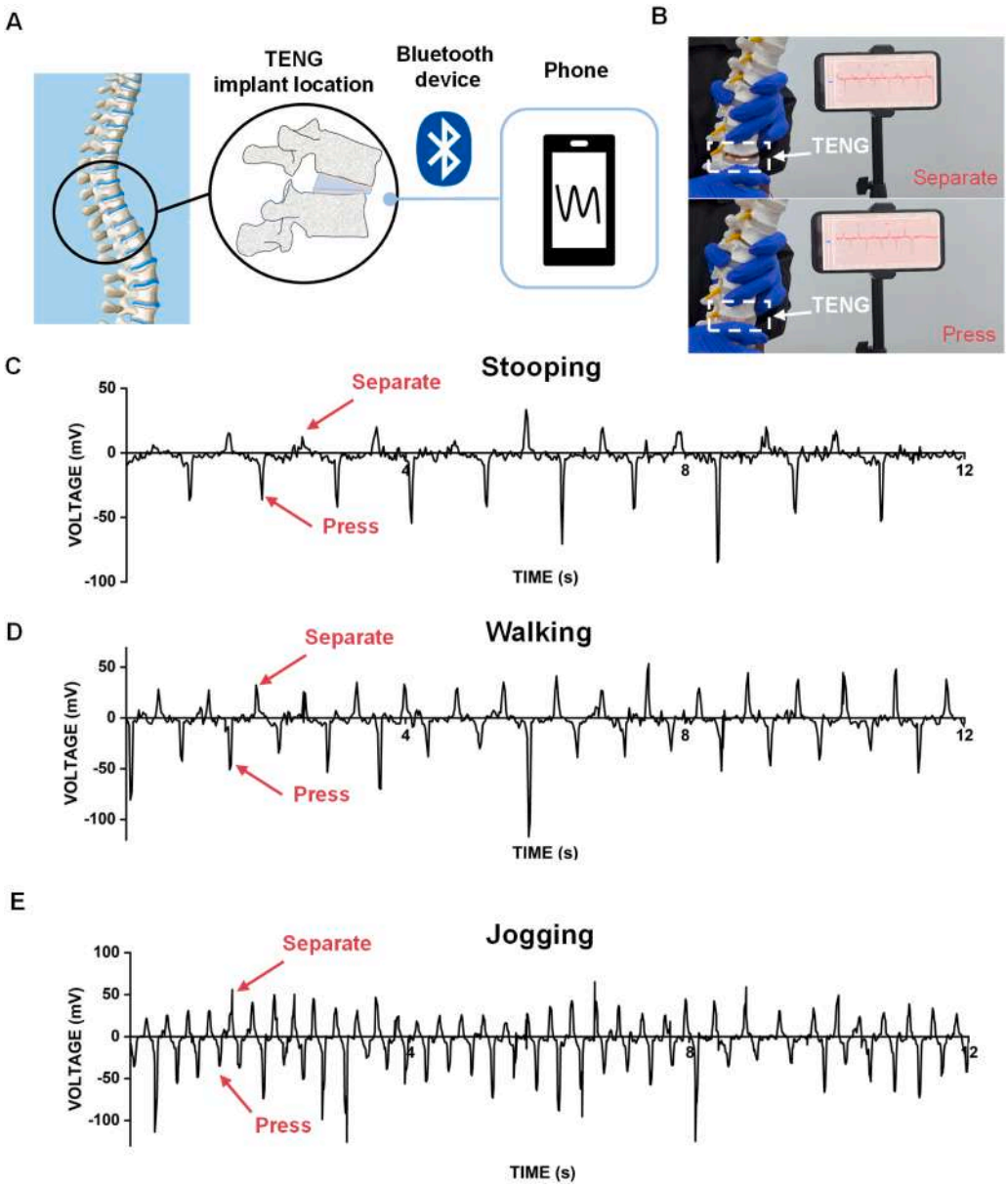

Fig. 8. A: Schematic diagram of the implantation position and wireless Bluetooth function of the TENG spinal motion monitor; B: Spinal motion simulation test; C: TENG voltage signal when bending; D: TENG voltage signal when walking; E: TENG voltage signal when jogging.

output voltage, allowing for precise monitoring of spinal motion during spinal cord injury rehabilitation.

Moreover, the TENG can be connected to wireless devices to transmit signals to a mobile phone, facilitating real-time monitoring of spinal movements. This capability is crucial for the timely diagnosis of secondary spinal injuries and for assessing the integrity of the neurostimulator.

3. Conclusion

This study introduces a next-generation neural stimulator, specifically designed as a fully implantable, flexible device that is wirelessly powered and mechanically compatible with biological tissues. Focusing on spinal cord neural stimulation, we developed a stimulation device tailored for spinal tissue. The mechanical performance of the electrodes was optimized using a serpentine fractal structure to align with the tensile stress-strain curve of spinal tissue, enhancing the mechanical compatibility between the electrodes and the spinal tissue. Notably, the electrode's resistance exhibited minimal variation under significant deformation(70 %), demonstrating stability under load. To circumvent transcutaneous circuitry and reduce the risk of complications and secondary infections, we employed wireless inductive power transfer for energy reception. The device is encapsulated with PDMS, ensuring compatibility with biological tissues. Experimental results indicate that, after 21 days of implantation, blind pathological histological evaluations confirm the biocompatibility of the implanted device. Furthermore, we integrated a flexible spinal motion detector based on a triboelectric nanogenerator (TENG) with the neural stimulator. This spinal motion monitor demonstrated robust electrical signal output. Conceptual experiments illustrated that the TENG-based monitor could generate varying voltage signals corresponding to different physical activities, with real-time monitoring capabilities via Bluetooth transmission to mobile devices. In summary, we have successfully integrated spinal cord neural stimulation with spinal motion monitoring into a single device that is soft, lightweight, biocompatible, and mechanically matched to biological tissues. The entire system is fully implantable and

operates wirelessly, with both neural stimulation and motion monitoring functions independent of external wiring.

CRediT authorship contribution statement

Peng Zhao: Writing – original draft, Methodology, Investigation, Formal analysis, Data curation, Conceptualization. **Niu Zhaoxuan:** Methodology, Formal analysis, Data curation. **Leng Jinsong:** Supervision, Resources, Project administration, Funding acquisition. **Liu Yanju:** Supervision, Resources, Funding acquisition. **Zeng Chengjun:** Writing – review & editing, Methodology. **Zhao Wei:** Writing – review & editing, Writing – original draft, Supervision, Methodology, Funding acquisition, Conceptualization.

Declaration of Competing Interest

The authors declare that they have no known competing financial interests or personal relationships that could have appeared to influence the work reported in this paper.

Acknowledgments

This work is supported by the National Key R&D Program of China (2022YFB3805700, 2024YFB4710205), National Natural Science Foundation of China (Grant No. 12472147, U23A20412, 12402160), the Research Fund of State Key Laboratory of Mechanics and Control for Aerospace Structures (Nanjing University of Aeronautics and astronautics) (Grant No. MCAS-E-0224G02), and Young Elite Scientists Sponsorship Program by CAST (Grant No. 2023QNRC001), Heilongjiang Provincial Natural Science Foundation of China 2022ZX02C25.

Appendix A. Supporting information

Supplementary data associated with this article can be found in the online version at doi:10.1016/j.nanoen.2025.110895.

Data availability

Data will be made available on request.

References

[1] A. Kralj, T. Bajd, Functional Electrical Stimulation: Standing and Walking After Spinal Cord Injury, Routledge, New York, 2022, https://doi.org/10.1201/9780203755402.
[2] J. Lo, L. Chan, S. Flynn, A systematic review of the incidence, prevalence, costs, and activity and work limitations of amputation, osteoarthritis, rheumatoid arthritis, back pain, multiple sclerosis, spinal cord injury, stroke, and traumatic brain injury in the united states: a 2019 update, Arch. Phys. Med. Rehabil. 102 (2021) 115–131, https://doi.org/10.1016/j.apmr.2020.04.001.
[3] Y. Ma, Y. Zhang, S. Cai, Z. Han, X. Liu, F. Wang, Y. Cao, Z. Wang, H. Li, Y. Chen, X. Feng, Flexible hybrid electronics for digital healthcare, Adv. Mater. 32 (2020) 1902062, https://doi.org/10.1002/adma.201902062.
[4] D. Wirthl, R. Pichler, M. Drack, G. Kettlguber, R. Moser, R. Gerstmayr, F. Hartmann, E. Bradt, R. Kaltseis, C.M. Siket, S.E. Schausberger, S. Hild, S. Bauer, M. Kaltenbrunner, Instant tough bonding of hydrogels for soft machines and electronics, Sci. Adv. 3 (2017) e1700053, https://doi.org/10.1126/sciadv.1700053.
[5] H. Jin, N. Matsuhisa, S. Lee, M. Abbas, T. Yokota, T. Someya, Enhancing the performance of stretchable conductors for E-textiles by controlled ink permeation, Adv. Mater. 29 (2017) 1605848, https://doi.org/10.1002/adma.201605848.
[6] M.D. Dickey, Stretchable and soft electronics using liquid metals, Adv. Mater. 29 (2017) 1606425, https://doi.org/10.1002/adma.201606425.
[7] A.D. Valentine, T.A. Busbee, J.W. Boley, J.R. Raney, A. Chortos, A. Kotikian, J. D. Berrigan, M.F. Durstock, J.A. Lewis, Hybrid 3D printing of soft electronics, Adv. Mater. 29 (2017) 1703817, https://doi.org/10.1002/adma.201703817.
[8] H. Lorach, A. Galvez, V. Spagnolo, F. Martel, S. Karakas, N. Intering, M. Vat, O. Faivre, C. Harte, S. Komi, J. Ravier, T. Collin, L. Coquoz, I. Sakr, E. Baaklini, S. D. Hernandez-Charpak, G. Dumont, R. Buschman, N. Buse, T. Denison, I. van Nes, L. Asboth, A. Watrin, L. Struber, F. Sauter-Starace, L. Langar, V. Auboiroux, S. Carda, S. Chabardes, T. Aksenova, R. Demesmaeker, G. Charvet, J. Bloch, G. Courtine, Walking naturally after spinal cord injury using a brain–spine interface, Nature 618 (2023) 126–133, https://doi.org/10.1038/s41586-023-06094-5.
[9] A. Rowald, S. Komi, R. Demesmaeker, E. Baaklini, S.D. Hernandez-Charpak, E. Paoles, H. Montanaro, A. Cassara, F. Becce, B. Lloyd, T. Newton, J. Ravier, N. Kinany, M. D'Ercole, A. Paley, N. Hankov, C. Varescon, L. McCracken, M. Vat, M. Caban, A. Watrin, C. Jacquet, L. Bole-Feysot, C. Harte, H. Lorach, A. Galvez, M. Tschopp, N. Herrmann, M. Wacker, L. Geernaert, I. Fodor, V. Radevich, K. Van Den Keybus, G. Eberle, E. Pralong, M. Roulet, J.-B. Ledoux, E. Fornari, S. Mandija, L. Mattera, R. Martuzzi, B. Nazarian, S. Benkler, S. Callegari, N. Greiner, B. Fuhrer, M. Froeling, N. Buse, T. Denison, R. Buschman, C. Wende, D. Ganty, J. Bakker, V. Delattre, H. Lambert, K. Minassian, C.A.T. van den Berg, A. Kavounoudias, S. Micera, D. Van De Ville, Q. Barraud, E. Kurt, N. Kuster, E. Neufeld, M. Capogrosso, L. Asboth, F.B. Wagner, J. Bloch, G. Courtine, Activity-dependent spinal cord neuromodulation rapidly restores trunk and leg motor functions after complete paralysis, Nat. Med. 28 (2022) 260–271, https://doi.org/10.1038/s41591-021-01663-5.
[10] N. Greiner, B. Barra, G. Schiavone, H. Lorach, N. James, S. Conti, M. Kaeser, F. Fallegger, S. Borgognon, S. Lacour, J. Bloch, G. Courtine, M. Capogrosso, Recruitment of upper-limb motoneurons with epidural electrical stimulation of the cervical spinal cord, Nat. Commun. 12 (2021) 435, https://doi.org/10.1038/s41467-020-20703-1.
[11] S.K. Patel, Y.M. Gozal, M.S. Saleh, J.L. Gibson, M. Karsy, G.T. Mandybur, Spinal cord stimulation failure: evaluation of factors underlying hardware explantation, J. Neurosurg. Spine 32 (2019) 133–138, https://doi.org/10.3171/2019.6.SPINE181099.
[12] N. Kazem, M.D. Bartlett, C. Majidi, Extreme toughening of soft materials with liquid metal, Adv. Mater. 30 (2018) 1706594, https://doi.org/10.1002/adma.201706594.
[13] M.D. Bartlett, A. Fassler, N. Kazem, E.J. Markvicka, P. Mandal, C. Majidi, Stretchable, high-k dielectric elastomers through liquid-metal inclusions, Adv. Mater. 28 (2016) 3726–3731, https://doi.org/10.1002/adma.201506243.
[14] Z. Xue, H. Song, J.A. Rogers, Y. Zhang, Y. Huang, Mechanically-guided structural designs in stretchable inorganic electronics, Adv. Mater. 32 (2020) 1902254, https://doi.org/10.1002/adma.201902254.
[15] A.C. Nanivadekar, R. Bose, B.A. Petersen, E.V. Okorokova, D. Sarma, T. J. Madonna, B. Barra, J. Farooqui, A.N. Dalrymple, I. Levy, E.R. Helm, V.J. Miele, M.L. Boninger, M. Capogrosso, S.J. Bensmaia, D.J. Weber, L.E. Fisher, Restoration of sensory feedback from the foot and reduction of phantom limb pain via closed-loop spinal cord stimulation, Nat. Biomed. Eng. 8 (2024) 992–1003, https://doi.org/10.1038/s41551-023-01153-8.
[16] I. Peña Pino, C. Hoover, S. Venkatesh, A. Ahmadi, D. Sturtevant, N. Patrick, D. Freeman, A. Parr, U. Samadani, D. Balser, A. Krassioukov, A. Phillips, T.I. Netoff, D. Darrow, Long-term spinal cord stimulation after chronic complete spinal cord injury enables volitional movement in the absence of stimulation, Front. Syst. Neurosci. 14 (2020), https://doi.org/10.3389/fnsys.2020.00035.
[17] A. Abd-Elsayed, C. Gilligan, BurstDR™ spinal cord stimulation for non-operated discogenic low back pain, Pain. Pract. 23 (2023) 563–565, https://doi.org/10.1111/papr.13210.
[18] W. Lee, T. Someya, Emerging trends in flexible active multielectrode arrays, Chem. Mater. 31 (2019) 6347–6358, https://doi.org/10.1021/acs.chemmater.9b00165.
[19] M.A. González-González, A. Kanneganti, A. Joshi-Imre, A.G. Hernandez-Reynoso, G. Bendale, R. Modi, M. Ecker, A. Khurram, S.F. Cogan, W.E. Voit, M.I. Romero-Ortega, Thin film multi-electrode softening cuffs for selective neuromodulation, Sci. Rep. 8 (2018) 16390, https://doi.org/10.1038/s41598-018-34566-6.
[20] Y. Zhang, N. Zheng, Y. Cao, F. Wang, P. Wang, Y. Ma, B. Lu, G. Hou, Z. Fang, Z. Liang, M. Yue, Y. Li, Y. Chen, J. Fu, J. Wu, T. Xie, X. Feng, Climbing-inspired twining electrodes using shape memory for peripheral nerve stimulation and recording, Sci. Adv. 5 (2019) eaaw1066, https://doi.org/10.1126/sciadv.aaw1066.
[21] I.R. Minev, P. Musienko, A. Hirsch, Q. Barraud, N. Wenger, E.M. Moraud, J. Gandar, M. Capogrosso, T. Milekovic, L. Asboth, R.F. Torres, N. Vachicouras, Q. Liu, N. Pavlova, S. Duis, A. Larmagnac, J. Vörös, S. Micera, Z. Suo, G. Courtine, S.P. Lacour, Electronic dura mater for long-term multimodal neural interfaces, Science 347 (2015) 159–163, https://doi.org/10.1126/science.1260318.
[22] W. Zhao, H. Ni, C. Ding, L. Liu, Q. Fu, F. Lin, F. Tian, P. Yang, S. Liu, W. He, X. Wang, W. Huang, Q. Zhao, 2D Titanium carbide printed flexible ultrawideband monopole antenna for wireless communications, Nat. Commun. 14 (2023) 278, https://doi.org/10.1038/s41467-022-35371-6.
[23] C. Yang, Q. Wu, J. Liu, J. Mo, X. Li, C. Yang, Z. Liu, J. Yang, L. Jiang, W. Chen, H. Chen, J. Wang, X. Xie, Intelligent wireless theranostic contact lens for electrical sensing and regulation of intraocular pressure, Nat. Commun. 13 (2022) 2556, https://doi.org/10.1038/s41467-022-29860-x.
[24] S. Mishra, Y.-S. Kim, J. Intarasirisawat, Y.-T. Kwon, Y. Lee, M. Mahmood, H.-R. Lim, R. Herbert, K.J. Yu, C.S. Ang, W.-H. Yeo, Soft, wireless periocular wearable electronics for real-time detection of eye vergence in a virtual reality toward mobile eye therapies, Sci. Adv. 6 (2020) eaay1729, https://doi.org/10.1126/sciadv.aay1729.
[25] A. Burton, Z. Wang, D. Song, S. Tran, J. Hanna, D. Ahmad, J. Bakall, D. Clausen, J. Anderson, R. Peralta, K. Sandepudi, A. Benedetto, E. Yang, D. Basrai, L.E. Miller, M.C. Tresch, P. Gutruf, Fully implanted battery-free high power platform for chronic spinal and muscular functional electrical stimulation, Nat. Commun. 14 (2023) 1–17, https://doi.org/10.1038/s41467-023-43669-2.
[26] C. Li, D. Liu, C. Xu, Z. Wang, S. Shu, Z. Sun, W. Tang, Z.L. Wang, Sensing of joint and spinal bending or stretching via a retractable and wearable badge reel, Nat. Commun. 12 (2021) 2950, https://doi.org/10.1038/s41467-021-23207-8.

[27] R.R. Gomes Costa, J.R. Dorneles, J.H.C.L. Veloso, C.W.P. Gonçalves, F.R. Neto, Feasibility and validity of the push-up test for synchronous and asynchronous strength tele-assessment in spinal cord injury individuals with paraplegia, J. Spinal Cord. Med. 47 (2024) 530–539, https://doi.org/10.1080/10790268.2022.2124651.
[28] H. Saito, Y. Watanabe, T. Kutsuna, T. Futohashi, Y. Kusumoto, H. Chiba, M. Kubo, H. Takasaki, Spinal movement variability associated with low back pain: a scoping review, PLOS One 16 (2021) e0252141, https://doi.org/10.1371/journal.pone.0252141.
[29] C. Li, D. Liu, C. Xu, Z. Wang, S. Shu, Z. Sun, W. Tang, Z.L. Wang, Sensing of joint and spinal bending or stretching via a retractable and wearable badge reel, Nat. Commun. 12 (2021) 2950, https://doi.org/10.1038/s41467-021-23207-8.
[30] S.S. Hlaing, R. Puntumetakul, E.E. Khine, R. Boucaut, Effects of core stabilization exercise and strengthening exercise on proprioception, balance, muscle thickness and pain related outcomes in patients with subacute nonspecific low back pain: a randomized controlled trial, BMC Musculoskelet. Disord. 22 (2021) 998, https://doi.org/10.1186/s12891-021-04858-6.
[31] G. Liu, G.J. Zhang, F. Jiang, X.D. Ding, Y.J. Sun, J. Sun, E. Ma, Nanostructured high-strength molybdenum alloys with unprecedented tensile ductility, Nat. Mater. 12 (2013) 344–350, https://doi.org/10.1038/nmat3544.
[32] A.M. Ribeiro, T.H.S. Flores-Sahagun, R.C. Paredes, A perspective on molybdenum biocompatibility and antimicrobial activity for applications in implants, J. Mater. Sci. 51 (2016) 2806–2816, https://doi.org/10.1007/s10853-015-9664-y.
[33] O.A. Araromi, M.A. Graule, K.L. Dorsey, S. Castellanos, J.R. Foster, W.-H. Hsu, A. E. Passy, J.J. Vlassak, J.C. Weaver, C.J. Walsh, R.J. Wood, Ultra-sensitive and resilient compliant strain gauges for soft machines, Nature 587 (2020) 219–224, https://doi.org/10.1038/s41586-020-2892-6.
[34] N. Li, W. Zhao, F. Li, L. Liu, Y. Liu, J. Leng, A 4D-printed programmable soft network with fractal design and adjustable hydrophobic performance, Matter 6 (2023) 940–962, https://doi.org/10.1016/j.matt.2022.12.010.
[35] Q. Ma, Y. Zhang, Mechanics of fractal-inspired horseshoe microstructures for applications in stretchable electronics, J. Appl. Mech. 83 (2016), https://doi.org/10.1115/1.4034458.
[36] D. Sturm, M. Heilmaier, J.H. Schneibel, P. Jéhanno, B. Skrotzki, H. Saage, The influence of silicon on the strength and fracture toughness of molybdenum, Mater. Sci. Eng. A 463 (2007) 107–114, https://doi.org/10.1016/j.msea.2006.07.153.
[37] Z. Wu, C. Peng, J. Liao, Q. Chen, Study on circuit modeling of stretchable serpentine interconnects, Int. J. Circuit Theory Appl. 50 (2022) 988–996, https://doi.org/10.1002/cta.3174.
[38] Y. Tian, P. He, B. Yang, Z. Yi, L. Lu, J. Liu, A flexible piezoelectric strain sensor array with laser-patterned serpentine interconnects, IEEE Sens. J. 20 (2020) 8463–8468, https://doi.org/10.1109/JSEN.2020.2985063.
[39] Z. Han, Y. Hong, X. Zhu, X. Gu, Y. Sun, Electrical performance optimization of serpentine interconnect for stretchable electronics, J. Phys. Conf. Ser. 2342 (2022) 012005, https://doi.org/10.1088/1742-6596/2342/1/012005.
[40] C. Jin, J. Yu, R. Li, X. Ye, Regional biomechanical characterization of the spinal cord tissue: dynamic mechanical response, Front. Bioeng. Biotechnol. 12 (2024), https://doi.org/10.3389/fbioe.2024.1439323.
[41] S. Cavelier, R.D. Quarrington, C.F. Jones, Mechanical properties of porcine spinal dura mater and pericranium, J. Mech. Behav. Biomed. Mater. 126 (2022) 105056, https://doi.org/10.1016/j.jmbbm.2021.105056.
[42] A. Liston, R. Bayford, D. Holder, A cable theory based biophysical model of resistance change in crab peripheral nerve and human cerebral cortex during neuronal depolarisation: implications for electrical impedance tomography of fast neural activity in the brain, Med. Biol. Eng. Comput. 50 (2012) 425–437, https://doi.org/10.1007/s11517-012-0901-0.
[43] A. Kurs, A. Karalis, R. Moffatt, J.D. Joannopoulos, P. Fisher, M. Soljačić, Wireless power transfer via strongly coupled magnetic resonances, Science 317 (2007) 83–86, https://doi.org/10.1126/science.1143254.
[44] S.I. Babic, C. Akyel, Calculating mutual inductance between circular coils with inclined axes in air, IEEE Trans. Magn. 44 (2008) 1743–1750, https://doi.org/10.1109/TMAG.2008.920251.
[45] M. Bonizzato, N.D. James, G. Pidpruzhnykova, N. Pavlova, P. Shkorbatova, L. Baud, C. Martinez-Gonzalez, J.W. Squair, J. DiGiovanna, Q. Barraud, S. Micera, G. Courtine, Multi-pronged neuromodulation intervention engages the residual motor circuitry to facilitate walking in a rat model of spinal cord injury, Nat. Commun. 12 (2021) 1925, https://doi.org/10.1038/s41467-021-22137-9.
[46] S. Harkema, Y. Gerasimenko, J. Hodes, J. Burdick, C. Angeli, Y. Chen, C. Ferreira, A. Willhite, E. Rejc, R.G. Grossman, V.R. Edgerton, Effect of epidural stimulation of the lumbosacral spinal cord on voluntary movement, standing, and assisted stepping after motor complete paraplegia: a case study, Lancet 377 (2011) 1938–1947, https://doi.org/10.1016/S0140-6736(11)60547-3.
[47] M. Vöröslakos, Y. Takeuchi, K. Brinyiczki, T. Zombori, A. Oliva, A. Fernández-Ruiz, G. Kozák, Z.T. Kincses, B. Iványi, G. Buzsáki, A. Berényi, Direct effects of transcranial electric stimulation on brain circuits in rats and humans, Nat. Commun. 9 (2018) 483, https://doi.org/10.1038/s41467-018-02928-3.
[48] H.R. Siebner, K. Funke, A.S. Aberra, A. Antal, S. Bestmann, R. Chen, J. Classen, M. Davare, V. Di Lazzaro, P.T. Fox, M. Hallett, A.N. Karabanov, J. Kesselheim, M. M. Beck, G. Koch, D. Liebetanz, S. Meunier, C. Miniussi, W. Paulus, A.V. Peterchev, T. Popa, M.C. Ridding, A. Thielscher, U. Ziemann, J.C. Rothwell, Y. Ugawa, Transcranial magnetic stimulation of the brain: What is stimulated? – a consensus and critical position paper, Clin. Neurophysiol. 140 (2022) 59–97, https://doi.org/10.1016/j.clinph.2022.04.022.
[49] B.-Q. Lai, X. Zeng, W.-T. Han, M.-T. Che, Y. Ding, G. Li, Y.-S. Zeng, Stem cell-derived neuronal relay strategies and functional electrical stimulation for treatment of spinal cord injury, Biomaterials 279 (2021) 121211, https://doi.org/10.1016/j.biomaterials.2021.121211.
[50] J.P. Miller, S. Eldabe, E. Buchser, L.M. Johanek, Y. Guan, B. Linderoth, Parameters of spinal cord stimulation and their role in electrical charge delivery: a review, Neuromodul. Technol. Neural Interface 19 (2016) 373–384, https://doi.org/10.1111/ner.12438.
[51] S. Cao, Y. Wei, R. Bo, X. Yun, S. Xu, Y. Guan, J. Zhao, Y. Lan, B. Zhang, Y. Xiong, T. Jin, Y. Lai, J. Chang, Q. Zhao, M. Wei, Y. Shao, Q. Quan, Y. Zhang, Inversely engineered biomimetic flexible network scaffolds for soft tissue regeneration, Sci. Adv. 9 (2023) eadi8606, https://doi.org/10.1126/sciadv.adi8606.
[52] Q.H. Nguyen, Q.T. Hoai Ta, N. Tran, Review on the transformation of biomechanical energy to green energy using triboelectric and piezoelectric based smart materials, J. Clean. Prod. 371 (2022) 133702, https://doi.org/10.1016/j.jclepro.2022.133702.
[53] Z.L. Wang, Triboelectric nanogenerators as new energy technology for self-powered systems and as active mechanical and chemical sensors, ACS Nano 7 (2013) 9533–9557, https://doi.org/10.1021/nn404614z.
[54] Z. Niu, Q. Wang, J. Lu, Y. Hu, J. Huang, W. Zhao, Y. Liu, Y.-Z. Long, G. Han, Electrospun cellulose nanocrystals reinforced flexible sensing paper for triboelectric energy harvesting and dynamic self-powered tactile perception, Small 20 (2024) 2307810, https://doi.org/10.1002/smll.202307810.

Zhao Peng is currently a senior student in the School of Future Technology at the Harbin Institute of Technology (HIT) and will receive the B.S. degree in Engineering Mechanics from Harbin Institute of Technology, China in 2025.

Zhaoxuan Niu received his master degree from Northeast Forestry University (China) in 2024. He is currently a Ph.D. student in the School of Chemistry and Chemical Engineering at Harbin Institute of Technology (supervised by Prof. Yanju Liu). His research interests focus on flexible triboelectric nanogenerators based on smart materials and their applications on environmental sensing and energy harvesting.

Chengjun Zeng is currently employed at the Harbin Institute of Technology (HIT), China. He received his Ph.D. from the School of Astronautics at Harbin Institute of Technology. His research interests are concentrated on shape-memory polymer composites and 4D-printed intelligent structures.

Wei Zhao obtained his Ph.D. in mechanics from the Harbin Institute of Technology (HIT), China. His research interests are focused on smart materials and structures, metamaterial structures, energy harvesting, implantable medical devices, and so on.